JOURNAL OF PROPULSION AND POWER
Vol. , No. ,

Central and External Cathode Operations in a Diverging-Magnetic-Field Electrostatic Thruster

Daisuke Ichihara,* Yoshiya Nakagawa,† Akira Iwakawa,‡ and Akihiro Sasoh§
Nagoya University, Nagoya 464-8603, Japan

https://doi.org/10.2514/1.B37636

The effects of hollow cathode position on thrust performances of a diverging-magnetic-field electrostatic thruster, which had a diverging magnetic field between a ring anode and a hollow cathode, were investigated. The hollow cathode was located in either a central or an external configuration. Based on the discharge current and direct thrust measurements, electrostatic and magnetic hybrid plasma acceleration was observed in the central cathode operation and even in the external cathode operation especially when magnetic field strength was less than 315 mT. However, the operating points were different: low discharge voltage × large discharge current in the central cathode operation, and high discharge voltage × small discharge current in the external cathode operation. This difference comes from electron-Hall parameter; the estimated electron-Hall parameter was about 50 in the central cathode operation, which was much lower than that of 3000 in the external cathode operation. By combining electromagnetic acceleration, the generated thrust can increase even with lower electron-Hall parameter operation. As a result, similar thrust performances were achieved in both cathode positions. Because of the hybrid plasma acceleration method, thrust density reached 50 N/m^2, which is comparable or even higher than that of the conventional electrostatic thrusters.

Nomenclature

A_{eff}	=	effective probe collection area, m^2
B	=	magnetic field strength at the magnet center on the centerline, T
c, ψ_c	=	coefficient
E_i	=	ion beam energy, eV
e	=	elementary charge, C
F	=	thrust, N
$f_{c,e}$	=	electron cyclotron frequency, Hz
$f_{e,i}$	=	Coulomb collision frequency, Hz
g	=	gravitational acceleration, m/s^2
I_{sat}	=	ion saturation current, A
I_{sp}	=	specific impulse, s
J_d	=	discharge current, A
J_i	=	ion beam current, A
J_k	=	keeper current, A
j_i	=	ion beam current density, A/m^2
k	=	Boltzmann constant, $(\text{m}^2 \cdot \text{kg})/(\text{s}^2 \cdot \text{K})$
$\log \Lambda$	=	Coulomb logarithm
m_i	=	ion mass, kg
$\dot{m}_a$	=	anode mass flow rate, kg/s
$\dot{m}_c$	=	cathode mass flow rate, kg/s
$\dot{m}_t$	=	$(\equiv \dot{m}_a + \dot{m}_c)$ total mass flow rate, kg/s
n_e	=	electron number density, m^{-3}
P_a	=	$(\equiv J_d V_d)$ anode input power, W
R	=	swing arm length, m
r, φ, z	=	cylindrical coordinates
T_e	=	electron temperature, K
u_e	=	electron thermal velocity, m/s
V_d	=	discharge voltage, V
V_f	=	floating potential, V
V_k	=	keeper voltage, V
V_s	=	space potential, V
z_{probe}	=	probe axial position, m
α, α'	=	thrust coefficient
γ	=	secondary electron yield
ε_0	=	permittivity of vacuum, F/m
η	=	thrust efficiency
κ	=	density decrement in presheath
λ_D	=	Debye length, m
φ	=	azimuthal angle, deg
ϕ	=	peak energy of ion energy distribution function, eV

Subscripts

EM	=	electromagnetic
ES	=	electrostatic

Received 21 April 2019; revision received 21 August 2019; accepted for publication 16 October 2019; published online XX epubMonth XXXX. Copyright © 2019 by the American Institute of Aeronautics and Astronautics, Inc. All rights reserved. All requests for copying and permission to reprint should be submitted to CCC at www.copyright.com; employ the eISSN 1533-3876 to initiate your request. See also AIAA Rights and Permissions www.aiaa.org/randp.

*Research Associate, Department of Aerospace Engineering.
†Graduate Student, Department of Aerospace Engineering.
‡Lecturer, Department of Aerospace Engineering. Member AIAA.
§Professor, Department of Aerospace Engineering. Associate Fellow AIAA.

I. Introduction

ELECTRIC space propulsion has been used as the primary propulsion system for north-south station keeping [1], orbit rising [2], and deep-space exploration [3] due to its high specific impulse, which cannot be achieved by chemical propulsion. Electrostatic ion acceleration, used in ion thrusters and Hall thrusters, is suitable for high-specific-impulse operation because ions are accelerated without collisional energy dissipation. In ion thrusters, ions are extracted by applying more than 1 kV between electrode grids [4], whereas in Hall thrusters, ions are extracted from plasma without using grids.

An electric field is generated locally in the plasma by applying a magnetic field perpendicular to the electric field in the radial direction. Because the magnetically trapped electrons maintain electric field, the relative position of the electron source (typically, a hollow cathode) with respect to the applied magnetic field affects the ion beam characteristics [5]. Hofer et al. [6] studied the effects of the cathode position on operation characteristics of Hall thruster. Two positions of hollow cathode—one outside the outer magnetic pole piece and the other in an internally mounted configuration central to the inner magnetic core—were investigated under an identical magnetic field. The internal cathode operation reduced the radial electron pressure gradient and moderated the beam divergence. Ding et al. [7] changed the magnetic field configuration with a fixed position of hollow cathode. They demonstrated that, by setting the magnetic separatrix outside the hollow cathode, thrust performance was improved. These studies show that regardless of the hollow cathode's relative position with respect to the magnetic field, the axial electric field accelerates ions without collisions.

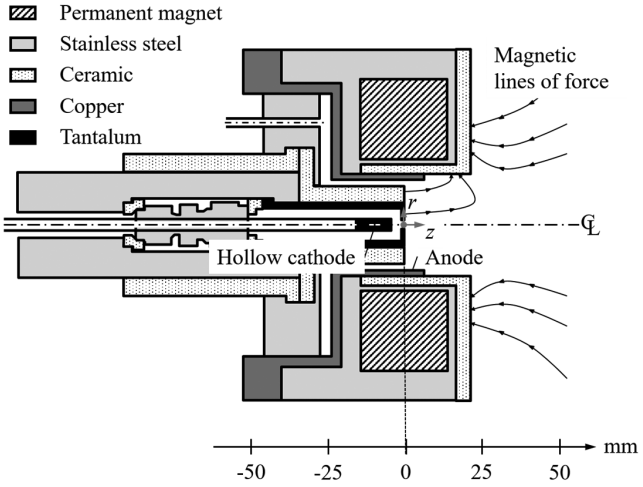

Fig. 1 Schematic of permanent-magnet diverging-magnetic-field electrostatic thruster with a central cathode (CC-EST).

Harada et al. [8] and Ichihara et al. [9] demonstrated electrostatic ion acceleration in an applied diverging magnetic field, where the hollow cathode is located at an off-axis, magnetic-field-free region in a downstream location. In the diverging magnetic field, the electron motion and electric field configuration are different from those in the electric field of a Hall thruster. They reported that the axial electric field was maintained near the exit of the applied diverging magnetic field. Sasoh et al. [10] set the hollow cathode at the center of the applied diverging magnetic field and obtained thrust characteristics of the electrostatic–magnetic hybrid plasma acceleration, in which the measured thrust was proportional to the anode mass flow rate as well as the electrostatic ion acceleration and was characterized by the Lorentz force assuming electromagnetic ion acceleration. Subsequently, they formulated the characteristic thrust of hybrid plasma acceleration and estimated the thrust coefficient of each electrostatic/magnetic acceleration [11]. These results indicate that for ion acceleration in the diverging magnetic field, relative position of the hollow cathode with respect to the magnetic field has a significant effect on ion acceleration mechanisms itself. Even though the position of the cathode has been studied, it was using different magnetic fields that could alter the effect of the cathode position. In this study, we examined the characteristics of thruster operation in an identical diverging magnetic field for both central and external position of the hollow cathode. We used an identical magnetic field to isolate the effect of position of the cathode and investigated the thruster operation characteristics. The thrust performance was related to the ion beam characteristics, and plasma properties were measured using electrostatic probes.

II. Experimental Setup

A. Thruster Head

Figure 1 shows a schematic of the permanent-magnet diverging-magnetic-field electrostatic thruster with a central cathode (CC-EST). The primary components are a permanent magnet, ring anode, and hollow cathode. An external magnetic field was applied by using a permanent ring magnet. The permanent magnet was packed in a housing fabricated with stainless steel (ISO: 4401-316-00-I), which, in turn, was protected from plasma with a ceramic (Photoveel) wall plate. The magnetic field strength at the center of the magnet was set

Table 1 Permanent magnets used for different magnetic field strengths

B, mT	Material	Inner dia., mm	Outer dia., mm	Length, mm
210	Neodymium	58	98	30
315	Samarium–cobalt	45	100	30
402	Neodymium	45	100	30

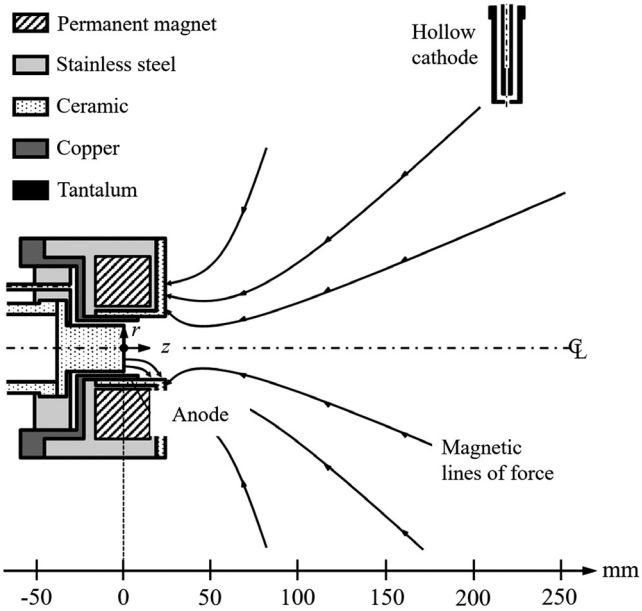

Fig. 2 Schematic of permanent-magnet diverging-magnetic-field electrostatic thruster with an external cathode (EC-EST).

to vary among three values, 210, 315, and 402 mT, by changing the permanent magnet size/material (summarized in Table 1). The applied magnetic field had a cusp around the thruster exit over the ceramic wall plate. The ring anode, which was fabricated using copper with an inner diameter of 30 mm and an effective length of 8 mm, was placed inside the permanent magnet. The hollow cathode (LHC-03-AE1-01; Kaufman & Robinson, Inc.) was located on the axis with its exit placed at the center of the permanent magnet. Between the ring anode and the hollow cathode, an insulating block fabricated with Photoveel was located. The propellant was fed through the 1.5-mm-thick slit between the ring anode's inner surface and the insulating block. The cylindrical coordinates (z, r), where z and r are the axial and radial coordinates, respectively, were defined in the axisymmetric configuration, with their origin at the center of the permanent magnet.

Figure 2 shows a schematic of the permanent-magnet diverging-magnetic-field electrostatic thruster with an external cathode (EC-EST; scale is not same as Fig. 1). The thruster head components were exactly the same as those for CC-EST, except the presence of the hollow cathode. Instead of the central hollow cathode, an insulating plate made in Photoveel was installed. In the preliminary thrust performance test, thrust and discharge current were measured with the fixed thruster operating condition, $\dot{m}_a = 1.4$ mg/s, $\dot{m}_c = 0.48$ mg/s, $B = 315$ mT, and $V_d = 250$ V, whereas the position of the hollow cathode was changed between 180 mm $\leq z \leq$ 220 mm, and 80 mm $\leq r \leq$ 200 mm. The position for maximum thrust efficiency revealed the hollow cathode position to be $(z, r) =$ (220 mm, 140 mm) as shown in Fig. 2. At this point, the magnetic field strength was less than 1 mT.

B. Vacuum Facility and Supplying Equipment

All experiments were conducted in a stainless (ISO: 4301-304-00-I) vacuum chamber 1.2 m in diameter and 3.2 m in length. The vacuum chamber was evacuated using a cryogenic pump (CRYO-U20; Ulvac Cryogenics, Inc.) with an exhaust speed of 8400 L/s, which was backed up by a dry pump (AA70WN-H; EBARA International Corp.) with an exhaust speed of 120 L/s. The chamber pressure was monitored by an ionization gauge (GI-TL3; ULVAC, Inc.). The base pressure of the system was less than 6×10^{-4} Pa and, during operation with a xenon flow of 0.7–4.8 mg/s, the chamber pressure remained in low-to-middle 10^{-2} Pa range.

Commercially available power supplies and mass-flow controllers were used for all experiments. A direct-current power supply (N8761A or N8935A; Agilent Technologies, Inc.) was used for the

main discharge power and the hollow cathode (KC8002; Kaufman & Robinson, Inc.). The main power supplies were operated in the constant-voltage mode. During thruster operation, the root-mean-square of V_d was less than 0.1% of the time-averaged value. On the other hand, the hollow cathode power supply was operated in the constant-current mode. The propellant and cathode operation gas, xenon (99.995% purity), was supplied through the mass flow controllers (3660 Series; Kofloc Co.) with an uncertainty of ± 0.1 mg/s.

C. Thrust and Plasma Diagnostics Measurements

1. Thrust Measurements

A pendulum-type thrust stand was used to measure the thrust directly. The thrust stand had a 300-mm-long stand arm supported by a two-knife-edge fulcrum. The knife edge was made of stainless steel (ISO: 4401-316-00-I), with a width of 10 mm and an apex angle of 90 deg. Each knife edge was mounted on a V-shaped groove with an opening angle of 120 deg. Each groove was formed by two blocks made of the same stainless steel as used in the knife edge so that the bottom was not rounded. The displacement of the pendulum was measured with a laser displacement sensor (IL-S025; Keyence Co.) at the tip of the aluminum extension arm, 128 mm away from the fulcrum. The solenoid actuator composed of a solenoid coil and a permanent magnet was used to keep a null displacement [12]. Therefore, the actuating force is equivalent to the thrust. The current for the solenoid actuator, supplied by the direct-current power supply (PWR-800L; Kikusui Electronics Co.), was regulated via proportional-integral-derivative (PID) control using a LabVIEW system. The thrust stand was calibrated up to 50 mN, using a pulley and weight arrangement driven by a direct-current motor at the same ambient pressure as during the thruster operations. The calibrated conversion factor from the solenoid current to the thrust was 20.7 mN/A. The thrust stand demonstrated a resolution of 0.2 mN, which was 6.2% of the minimum thrust value measured in this study. A "tare force" is an apparent thrust that should be corrected in the thrust measurement. As described in Ref. [13], the tare force was measured beforehand and was taken into account in the correction of thrust measurement. The tare force measurement uncertainty was 0.013 mN/A, which was 0.7% of the minimum thrust value measured in this study.

2. Ion Beam Current Measurements

Ion current and ion beam divergence half-angle were measured by a nude Faraday probe. The nude Faraday probe had an ion collector with an outer diameter of 12 mm on its center and a coaxial guard ring. The gap between the collector and the guard ring was 0.5 mm. In the horizontal plane on the central axis of the thrusters, the ion beam current density distribution was measured as a function of the azimuthal angle with respect to the central axis. A stepping motor (PK56; Oriental Motor Co., Ltd.) was used for the nude Faraday probe swinging, and the swing speed was 24 deg/s. The accuracy of the angular position was 0.1 deg. The rotation center was $(z, r) = (33\ \text{mm}, 0\ \text{mm})$, and length of the swing arm was 350 mm. Both the collector and the guard ring were negatively biased by 27 V with respect to the cathode potential. The ion current into the collector was measured using the voltage drop at a resistance of 1 kΩ ($\pm 5.0\%$ accuracy), connected in series to the nude Faraday probe circuit. Assuming an axisymmetric exhaust plume, the ion beam current is calculated as in Eq. (1):

$$J_\text{i} \equiv \int_{\varphi_2}^{\varphi_1} 2 j_\text{i}(\varphi) \pi R^2 |\sin\varphi| \, \text{d}\varphi / (1+\gamma) \tag{1}$$

where φ_1 and φ_2 are the swing ranges that were set in two types: $(\varphi_1, \varphi_2) = (-\pi/2, 0)$ and $(0, \pi/2)$. J_i was evaluated as the average of these two integrations. The J_i difference between swing directions was less than 1%; however, different limits of integration made a J_i difference of up to 10%, which was the main factor of the uncertainty. The secondary electron yield, γ, of the ion collector was 0.05 [14]. The ion beam divergence half-angle $\langle\varphi\rangle$ was calculated as the momentum-averaged value on the hemisphere face [15],

$$\cos\langle\varphi\rangle \equiv \int_{\varphi_2}^{\varphi_1} j_\text{i}(\varphi) |\sin\varphi| \cos\varphi \, \text{d}\varphi \Big/ \int_{\varphi_2}^{\varphi_1} j_\text{i}(\varphi) |\sin\varphi| \, \text{d}\varphi \tag{2}$$

Similar to the J_i calculation, $\langle\varphi\rangle$ was evaluated as the average value after setting $(\phi_1, \phi_2) = (-\pi/2, 0)$ and $(0, \pi/2)$ in Eq. (2). The uncertainty of $\cos\langle\varphi\rangle$ evaluation was up to 8% because of the difference of limits of integration.

The same three-grid retarding potential analyzer (RPA) used in Ref. [8] was used here to obtain the ion energy distribution function (IEDF). The three grids comprised a floating grid, electron repelling grid, and ion discriminator. The floating grid of the RPA was fixed at $(z, r) = (383\ \text{mm}, 0\ \text{mm})$. The collected ion current was measured by varying the potential of the ion discriminator, V_RPA, from -20 to 350 V with respect to the cathode potential. The collected ion current was fitted to a superimposition of Gaussian functions using the least-squares method. The IEDF was obtained by differentiating the fit curve with respect to V_RPA. The calculated IEDF had two distinct peaks at $V_\text{RPA} = \phi_1$ and $V_\text{RPA} = \phi_2$. The first and lower peak ϕ_1 corresponded to the space potential at the RPA location, whereas the second and higher peak ϕ_2 to the accelerated ion kinetic energy. Using ϕ_1 and ϕ_2, ion beam energy, E_i, was calculated by

$$E_i = \phi_2 - \phi_1 \tag{3}$$

3. Plasma Diagnostics

A double (electrostatic) probe was used for the measurements of electron temperature T_e and electron number density n_e. The probe tip was composed of two 0.3-mm-diam tungsten wires with an effective length of 3 mm. The separation distance between the wires was 2.2 mm. To obtain the probe current (I)–voltage (V) curve, the voltage between the two wires was varied between 6 and 20 Hz, and the probe current was measured using the same resistance as that used in the $j_i(\varphi)$ measurements. The measured I-V curve of the probe was fitted by a theoretical I-V expression for a symmetric double probe with the following sheath expansion [16]

$$I = I_\text{sat} \tanh\left(\frac{V}{2kT_e/e}\right) + c_1 V + c_2 \tag{4}$$

The coefficient c_1 corresponds to the sheath expansion in the ion saturation region, and c_2 reflects any offset currents owing to the stray capacitance [17]. The parameters I_sat, T_e, c_1, and c_2 were obtained as fitting parameters. As the double probe collects only the high-energy tail in the electron energy distribution, it is noted that the presented T_e value indicates that the plasma contained a single temperature corresponding to the higher energy distribution. The standard deviation of T_e fitting was up to 10%. Electron number density, n_e, was calculated using Eq. (6), which uses the Bohm approximation for the ion entry velocity to the sheath:

$$n_e = \frac{I_\text{sat}}{\kappa A_\text{eff}} \sqrt{\frac{m_i}{kT_e}} \tag{5}$$

The effective current collection area, A_eff, depends on the sheath thickness and was corrected using an iterative process based on the thin-sheath theorem [18]. Applying the low propagation of error in Eq. (6), the estimated uncertainty in n_e was $+8\%/-12\%$, which was the maximum.

A floating emissive probe was used for the plasma space potential, V_s, with respect to the cathode potential measurement. A 0.185-mm-diam wire fabricated using a 1% thoriated tungsten was bent into a semicircular shape with a diameter of 2.0 mm and was used for thermionic electron emission. The emission part was Joule-heated by supplying a heater current to emit a sufficient amount of thermionic electrons. When a heater current greater than 8.2 A was supplied, the probe floating voltage, V_f, became saturated. In this condition, the voltage drop at the thoriated tungsten wire was 6.0 V. To calculate V_s, the measured V_f was corrected by a factor of $\psi_c kT_e/e$ [19] as follows:

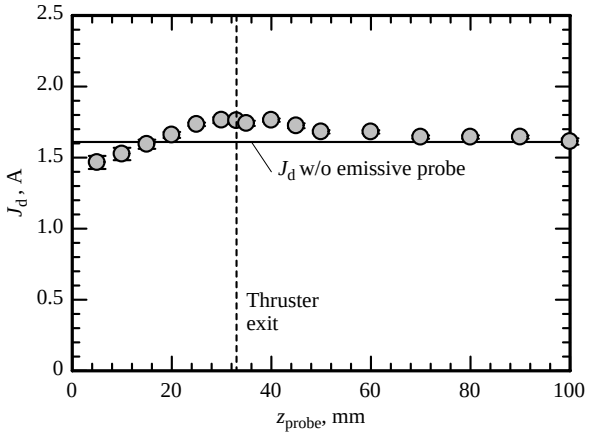

Fig. 3 Probe perturbation on J_d along the thruster central axis in EC operation, $\dot{m}_a = 1.4$ mg/s, $\dot{m}_c = 0.48$ mg/s, $B = 315$ mT, $V_d = 250$ V.

$$V_s = V_f + \psi_c kT_e/e \tag{6}$$

The correction factor, ψ_c, depends on the ratio of the Debye length to the filament radius and varies in $0 < \psi_c < 1.5$. From Eq. (6), the uncertainty in V_s is of the same order as the uncertainty in T_e. However, the potential drop at the heating part is also a source of uncertainty. Therefore, the uncertainty of V_s was $+0.6kT_e/e/-0.02kT_e/e \pm 3.0$ V.

The double probe and emissive probe were swept using the same stepping motor as used in the $j_i(\varphi)$ measurement with a sweep time shorter than 0.25 s at each point. The probe measurement position interval was at least 5 mm in the axial direction and 2.5 mm in the radial direction. In particular, inserting probes into a bulk plasma may cause nonnegligible perturbations to the thruster discharge [20]. The disturbances may influence thruster operation characteristics and plasma properties, especially around the probe location. The former effect can be characterized by the J_d variation. Figure 3 shows the measured J_d at each emissive probe measurement position along the thruster central axis ($r = 0$ mm) in the external cathode (EC) operation. By inserting the emissive probe in the downstream region ($z_{probe} > 70$ mm), the difference in J_d between with and without the operation of the emissive probe was less than $+2\%$. Later, the difference in J_d gradually increased and reached 9% at $z_{probe} = 33$ mm, at the thruster exit. At $z_{probe} < 33$ mm, the measured J_d decreased by 9% at $z_{probe} = 5$ mm. Thus, the probe insertion affected plasma properties. Staack et al. [21] reported that, owing to the secondary electron emission from the probe body, the inserted probe causes a decrease in electron temperature. The presented T_e value in this study can be an underestimate; however, we believe that these decreases did not affect the plasma parameter distributions critically.

III. Experimental Results

A. Operating Conditions

Operating conditions are summarized in Table 2. The uncertainties in B and J_d were ± 10 mT and ± 51 mA, respectively. A run under each operating condition was repeated at least three times while measuring F, J_d, E_i, and V_k. In the following figures, a symbol shows an averaged value for each operating condition. The error bars in F, J_d, and E_i represent the standard deviation ($\pm\sigma$) obtained after a number of trials, whereas the error bars in J_i and $\langle\varphi\rangle$ correspond to the uncertainty in the averaging. To minimize the effect of cathode temperature on the operation characteristics, we restricted the thruster running time within 10 s.

Table 2 Operating conditions

Symbol	Unit	Central cathode	External cathode
$\dot{m}_a$	mg/s	0.7–4.8	0.7–4.8
$\dot{m}_c$	mg/s	0.48	0.48
$\dot{m}_t$	mg/s	1.2–5.3	1.2–5.3
V_d	V	100–300	200–450
B	mT	210–402	210–402
J_k	A	2.0	2.0

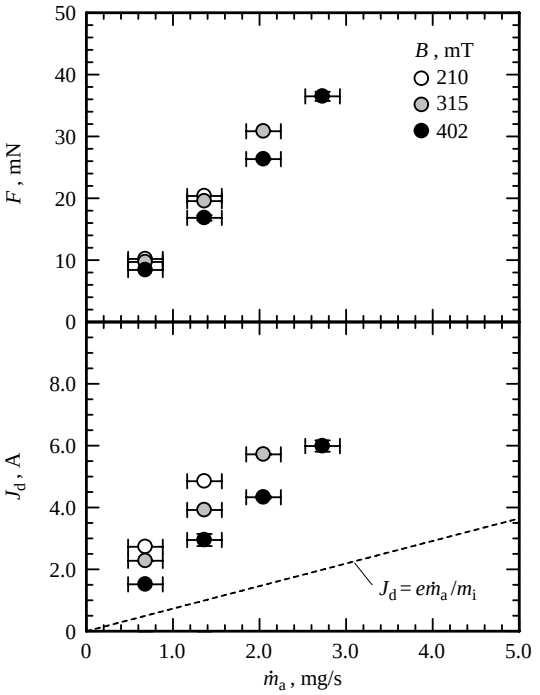

Fig. 4 $\dot{m}_a$ vs F and J_d with central cathode (CC-EST), $\dot{m}_c = 0.48$ mg/s, $V_d = 250$ V.

B. Thrust and Discharge Current Characteristics

Figure 4 shows $\dot{m}_a$ dependence of F and J_d with different B and a constant V_d of 250 V in CC operation. F and J_d almost linearly increased with increasing $\dot{m}_a$. For example, by increasing $\dot{m}_a$ from 0.7 to 2.0 mg/s with $B = 315$ mT, F and J_d increased from 9.7 to 30 mN and from 2.2 to 5.7 A, respectively. Both F and J_d showed a decrease with increasing B. Yet, the discharge current had a higher sensitivity to B than that of F. At $\dot{m}_a = 1.4$ mg/s, J_d decreased from 4.8 to 2.9 A by increasing B from 210 to 402 mT. Even for $B = 402$ mT, J_d was approximately three times higher than the ampere-equivalent anode flow rate, $e\dot{m}_a/m_i$.

On the other hand, EC operation showed different F and J_d dependencies on $\dot{m}_a$, as shown in Fig. 5. As with the case of CC operation, both F and J_d increased with increasing $\dot{m}_a$. However, at $\dot{m}_a = 1.4$ mg/s, for example, with increasing B, J_d decreased from 1.9 to 1.6 A and F slightly increased from 12 to 13 mN. EC operation suppressed J_d to less than half of that of the case of CC operation: by supplying $\dot{m}_a = 1.4$ mg/s and $B = 315$ mT, $J_d = 3.9$ A for CC operation, and 1.6 A for EC operation. Therefore, the J_d ratio to $e\dot{m}_a/m_i$ decreased to 1.6–2.0. In EC operation, more than 2.7 mg/s of $\dot{m}_a$ was necessary to thruster ignition with $B = 402$ mT. When $B = 402$ mT, F and J_d showed different dependence on $\dot{m}_a$ with respect to $B = 210$ and 402 mT case. By increasing B from 315 to 402 mT at $\dot{m}_a = 2.7$ mg/s, F decreased from 31 to 27 mN and J_d increased from 3.9 to 5.5 A.

Figure 6 shows the V_d dependence of F and J_d with different B and a constant $\dot{m}_a$ of 1.4 mg/s in CC operation. Both F and J_d increased gradually with increasing V_d. Particularly for $B = 402$ mT, by applying V_d greater than 200 V, J_d was almost saturated at 3.0 A, which is three times as large as $e\dot{m}_a/m_i$. In the J_d saturation region ($V_d > 200$ V), F was especially smaller than that of the other cases with $B = 210$ and 315 mT.

On the other hand, EC operation showed different V_d and B dependencies of F and J_d, as shown in Fig. 7. With increasing V_d, F increased but J_d remained small. At $B = 402$ mT, F increased from 18 to 24 mN, whereas J_d increased only by 0.3 A: from 2.5 to 2.8 A.

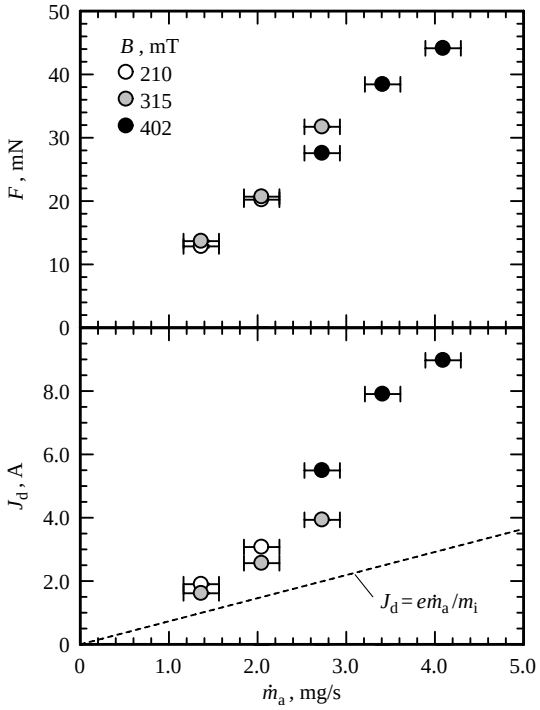

Fig. 5 $\dot{m}_a$ **vs** F **and** J_d **with external cathode (EC-EST),** $\dot{m}_c = 0.48$ **mg/s,** $V_d = 250$ **V.**

Combined with Fig. 5, J_d in an EC operation depends only on $\dot{m}_a$ and is not sensitive to V_d or B.

The experimentally obtained thrust should have contributions from the electrostatic and/or electromagnetic accelerations. As is described in detail in Ref. [11], the characteristic thrust for electrostatic acceleration is given by $\dot{m}_a(2eV_d/m_i)^{1/2}$ and for electromagnetic acceleration by J_dBR. The electrostatic thrust is expressed by

$$F = \alpha' m_a \sqrt{2eV_d/m_i} \tag{7}$$

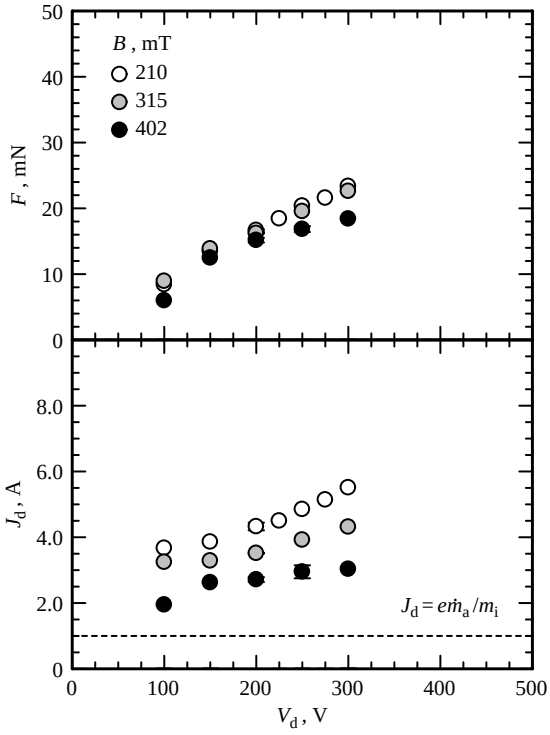

Fig. 6 V_d **vs** F **and** J_d **with CC-EST,** $\dot{m}_a = 1.4$ **mg/s,** $\dot{m}_c = 0.48$ **mg/s.**

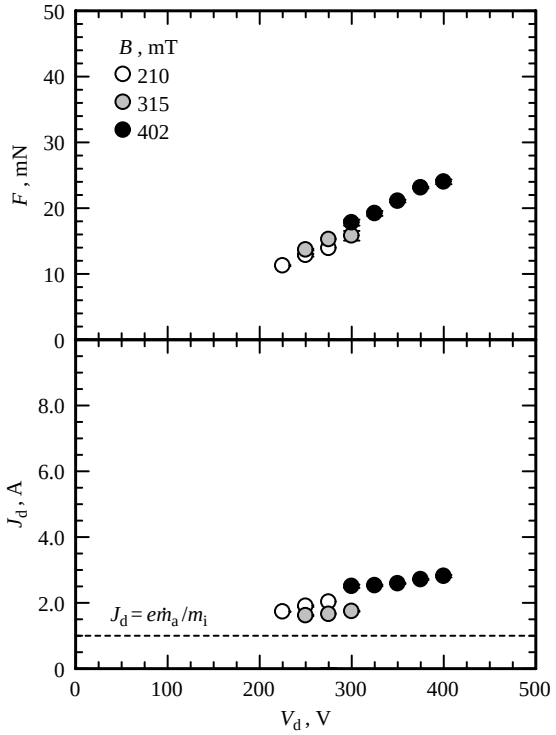

Fig. 7 V_d **vs** F **and** J_d **with EC-EST,** $\dot{m}_a = 1.4$ **mg/s,** $\dot{m}_c = 0.48$ **mg/s.**

In an ideal electrostatic acceleration for singly charged ions, α' is unity. While if the obtained thrust was generated by an electrostatic–magnetic hybrid acceleration, F should be expressed also using J_dBR. Sasoh et al. [11] formulated the thrust generated by this type of plasma acceleration in a diverging magnetic field.

$$F = \alpha J_d BR \tag{8}$$

$$\alpha \equiv \alpha_{\mathrm{ES}} + \alpha_{\mathrm{EM}} \tag{9}$$

where α_{ES} and α_{EM} are the thrust coefficients in electrostatic and electromagnetic acceleration, respectively. Because of the independency of electrostatic acceleration on the applied magnetic field, parameters α and α_{EM} are also related as

$$\alpha = c/B + \alpha_{\mathrm{EM}} \tag{10}$$

The calculated α at each B was fitted to Eq. (10) by using a least-squares method, and α_{EM} was estimated as a fitting parameter. $\alpha_{\mathrm{ES}} = c/B$ was calculated by subtracting α_{EM} from α.

Figures 8a and 8b show the thrust characteristics in CC operation. The error bars in $\dot{m}_a(2eV_d/m_i)^{1/2}$ and J_dBR come from the uncertainties of $\dot{m}_a$, V_d, J_d, and B, respectively. Regardless of operating conditions, F was almost proportional to both $\dot{m}_a(2eV_d/m_i)^{1/2}$ and J_dBR. The calculated α' using Eq. (7) is also shown in Fig. 8a. The obtained thrust fit well by Eq. (7) and B dependence was weak. Because of ion energy loss and beam diverging loss, experimentally fitted α' was less than unity. The calculated α values by using Eq. (8) are also shown in Fig. 8b. The thrust characteristics also fit well by Eq. (8), and α decreased with increasing B. This tendency indicates that both electrostatic and electromagnetic plasma accelerations contribute to generating thrust in CC operation.

Figures 9a and 9b show the thrust characteristics in EC operation. Just as CC operation, thrust in EC operation has weak B dependence and fit well by Eq. (7), whereas as shown in Fig. 9b, thrust with $B = 210$ and 315 mT fit well with Eq. (8) and the α value decreased with increasing B. When $B = 402$ mT, the thrust increased linearly with increasing J_dBR; however, the slope was changed at around $J_dBR = 15$ mN and the thrust did not follow Eq. (8). Hence, it is noted that the thrust generation mechanism in EC operation has B

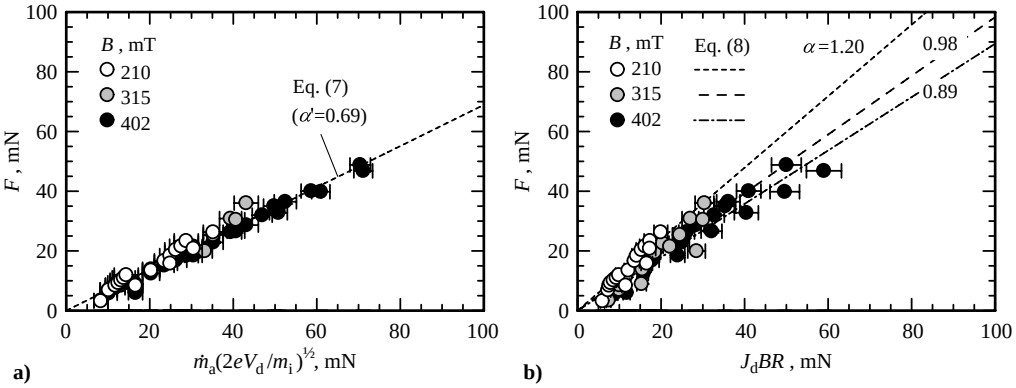

Fig. 8 Thrust characteristics with CC-EST: a) $\dot{m}_a(2eV_d/m_i)^{1/2}$ vs F; b) J_dBR vs F. Operating conditions are summarized in Table 2.

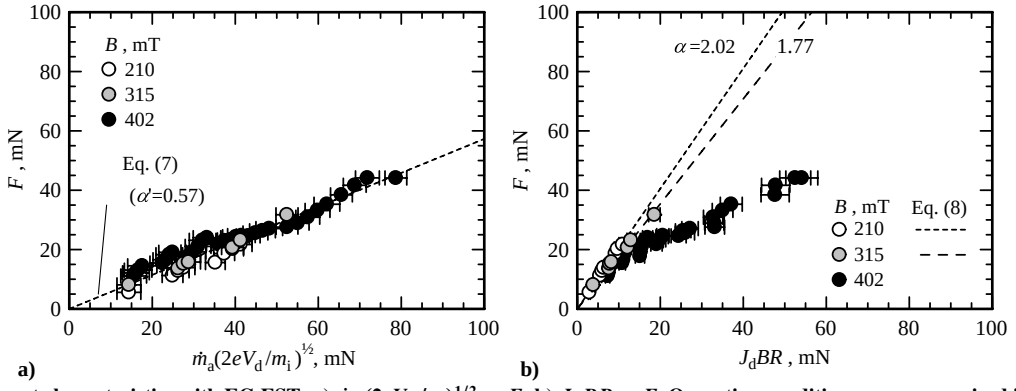

Fig. 9 Thrust characteristics with EC-EST: a) $\dot{m}_a(2eV_d/m)^{1/2}$ vs F; b) J_dBR vs F. Operating conditions are summarized in Table 2.

dependence. Within the experimental conditions, the electrostatic and electromagnetic plasma accelerations contribute to generating thrust for $B \leq 315$ mT, whereas for $B > 315$ mT, the electrostatic acceleration was dominant. Table 3 summarizes thrust coefficients. In both cathode positions, α exceeded 1.0, which means that the experimentally obtained thrust cannot be explained by only the electromagnetic acceleration. Moreover, in EC operation, the maximum α value was greater than 2.0, and this is 1.7 times higher than that of CC operation. In CC operation, the values of α_{EM} and α_{ES} were comparable, and the electromagnetic and electrostatic acceleration made the same level of contribution for thrust generation. In EC operation, α_{EM} was higher than α_{ES}. As shown in Fig. 2, electrons emitted from the hollow cathode must cross the magnetic lines of force before flowing into the anode. Through this transverse motion, electrons interact with the magnetic field and generate the Lorentz force. As a result, α_{EM} has a large value, even with EC setting.

C. Efficiency Analysis

From the measured thrust and other operation data (e.g., discharge voltage, current, mass flow rate), the specific impulse and thrust efficiency were calculated as

$$I_{sp} \equiv \frac{F}{\dot{m}_a g} \tag{11}$$

$$\eta \equiv \frac{F^2}{2\dot{m}_a P_a} \tag{12}$$

Table 3 Thrust coefficients

Cathode position	B, mT	α'	α	α_{EM}	α_{ES}
CC	210–402	0.69	0.89–1.20	0.64	0.25–0.56
EC	210, 315	0.57	1.77–2.02	1.26	0.51–0.76
	402	0.57	— —	— —	— —

Because $\dot{m}_a$ dominated the characteristics of F and J_d (see Figs. 4 and 5), I_{sp}, η, and specific power were evaluated based on $\dot{m}_a$ and anode input power P_a. Given the uncertainty in F, $\dot{m}_a$, J_d, and V_d, the relative uncertainty of I_{sp} and η was calculated as $\pm 4.6\%$ and $\pm 7.6\%$, respectively, based on the low propagation of error. Figure 10 shows $P_a/\dot{m}_a$ dependence of I_{sp} and η with different cathode positions. The value $P_a/\dot{m}_a$ indicates the specific input energy for propellant. Regardless of the cathode position, the obtained I_{sp} overlapped and increased with increasing $P_a/\dot{m}_a$. Both cathode positions showed the same maximum I_{sp} of 1800 s at $P_a/\dot{m}_a = 940$ MJ/kg in CC operation, and $P_a/\dot{m}_a = 820$ MJ/kg in EC operation. At these operating points, η also reached maximum value of 16% in CC operation and 19% in EC operation.

Figure 11 shows the V_d dependence of $J_i/(e\dot{m}_t/m_i)$ and J_i/J_d with different cathode positions. Assuming that the supplied propellant ionized only to a singly charged ion, $J_i/(e\dot{m}_t/m_i)$ is equal to the propellant utilization efficiency. Regardless of the hollow cathode position, $J_i/(e\dot{m}_t/m_i)$ increased with increasing V_d. As shown in Figs. 6 and 7, J_d increased with increasing V_d. Hence, input power increased with increasing V_d. Because η was maintained constant, the electron temperature and, thereby, the electron-impact ionization rate should increase with increasing V_d. In CC operation, the maximum $J_i/(e\dot{m}_t/m_i)$ was 1.2. The cause for this excess value has not been clearly identified; it could be due to the doubly charged ions or other reasons. However, the basic conclusions obtained from the present experiments are believed to remain valid. The V_d dependence of J_i/J_d is also shown in Fig. 11. The J_i/J_d value had been determined by the hollow cathode position, and within the same cathode position, J_i/J_d had no dependence on $\dot{m}_a$ and V_d because both J_d and $J_i/(e\dot{m}_t/m_i)$ increased with increasing V_d. With increasing V_d, J_i/J_d was maintained constant at 0.38 and 0.70 for CC and EC operation, respectively.

Figures 12a and 12b show the calculated IEDF and the V_d dependence of E_i, respectively. In both cathode positions, the calculated IEDF had two peaks. In the case of Fig. 12a, the first peak energy was 17 and 20 V for CC and EC operation, respectively.

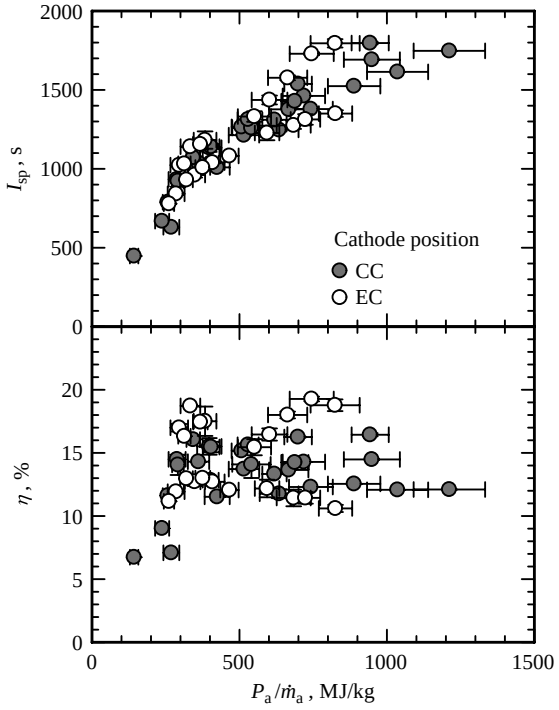

Fig. 10 $P_a/\dot{m}_a$ vs I_{sp} and η with different cathode positions, $\dot{m}_a = 1.4$ and 2.0 mg/s, $\dot{m}_c = 0.48$ mg/s, $B = 210$–405 mT, $V_d = 100$–400 V.

The second peak corresponds to the accelerated ion energy, which was 105 and 153 V for CC and EC operation, respectively. CC operation had a broader distribution than that of EC operation. From Fig. 12b, E_i of EC operation exhibited a higher value than that of CC operation. The voltage utilization efficiency E_i/V_d was 0.35 for CC operation and 0.57 for EC operation. Although the thruster operating condition was limited in EC operation, E_i/V_d maintained a constant value with increasing V_d, and E_i/V_d of CC operation maintained a lower level.

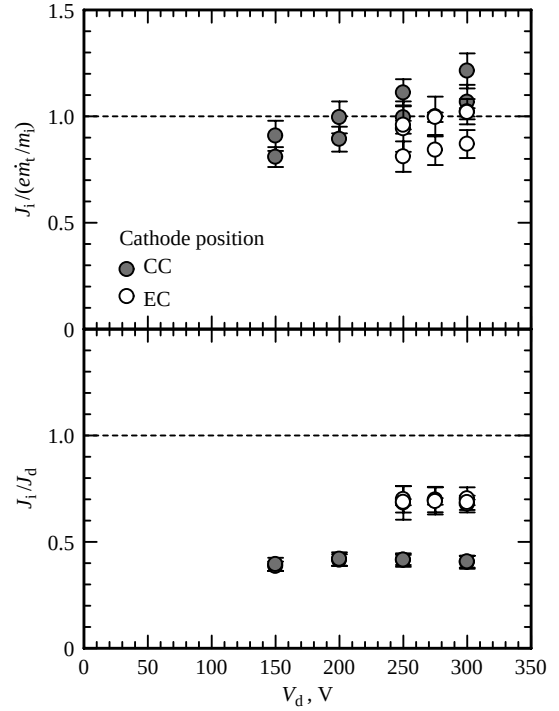

Fig. 11 V_d vs $J_i/(e\dot{m}_i/m_i)$ and J_i/J_d with different cathode positions, $\dot{m}_a = 1.4$ and 2.0 mg/s, $\dot{m}_c = 0.48$ mg/s, $B = 315$ mT, $V_d = 150$–300 V.

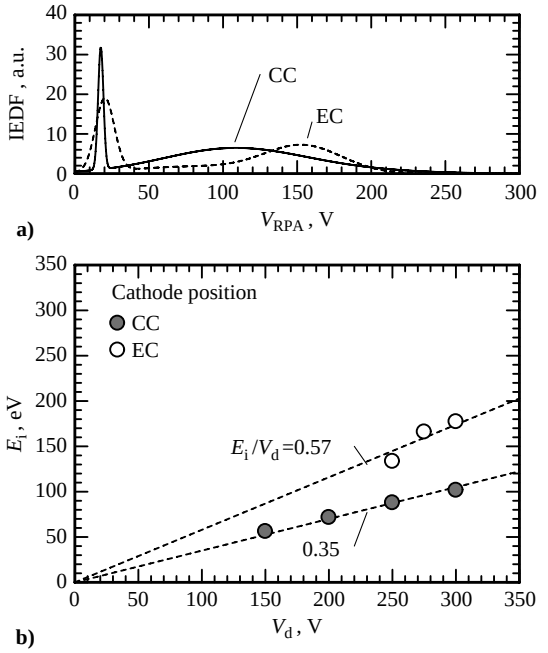

Fig. 12 Ion beam energy characteristics with different cathode positions: a) calculated IEDF in $\dot{m}_a = 1.4$ mg/s, $V_d = 250$ V; b) V_d vs E_i/V_d in $\dot{m}_a = 1.4$ mg/s, $\dot{m}_c = 0.48$ mg/s, $B = 315$ mT, $V_d = 150$–300 V.

Figures 13a and 13b show angular j_i distribution and the V_d dependence of the calculated $\langle\varphi\rangle$, based on Eq. (2) with different cathode positions, respectively. If the exhausted ion beam was absolutely axial symmetry, j_i distribution should also be symmetric with respect to the thruster central axis ($\varphi = 0$ deg). In CC operation, j_i had a single peak value of 8.2 A/cm^2 around $\varphi = 0$ deg and then monotonically decreased with increasing $|\varphi|$. On the other hand, EC operation had two local peaks of 3.7 A/cm^2 at 32 deg and 3.9 A/cm^2 at −40 deg. However, as we mentioned in the previous section, this asymmetry made an uncertainty with less than 8% of $\langle\varphi\rangle$ calculation and the presented $\langle\varphi\rangle$ were evaluated under this uncertainties. As shown in Fig. 13b, the $\langle\varphi\rangle$ of CC operation was smaller than that of EC operation by 7 deg. In CC operation, $\langle\varphi\rangle$

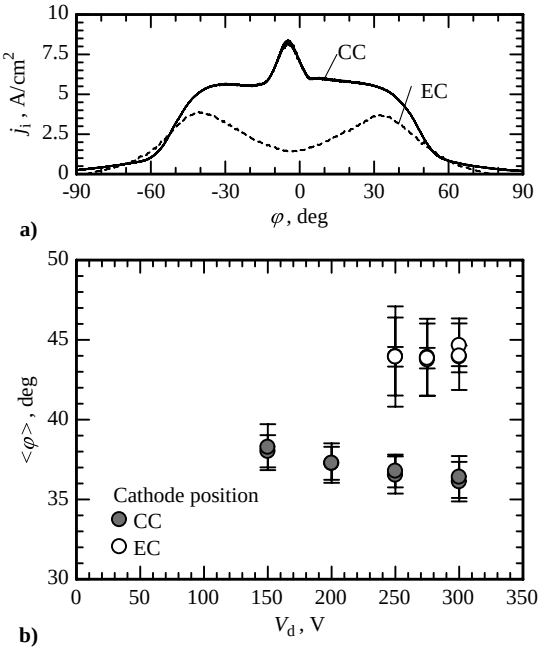

Fig. 13 Ion beam divergence half-angle with different cathode positions: a) φ vs j_i in $\dot{m}_a = 1.4$ mg/s, $V_d = 250$ V; b) V_d vs $\langle\varphi\rangle$ in $\dot{m}_a = 1.4$ and 2.0 mg/s, $\dot{m}_c = 0.48$ mg/s, $B = 315$ mT, $V_d = 150$–300 V.

decreased from 38 to 36 deg with increasing V_d. However, in EC operation, it maintained constant at 44 deg, varying not greater than ± 1 deg. The $j_i(\varphi)$ distribution is also related to the electromagnetic thrust generation. In the rigid-rotator model, electromagnetic thrust is proportional to the plasma rotation radius [22]. The j_i peak at off-axis angle indicates that the rotation radius corresponds to the peak angle (30–40 deg). The estimated rotation radius is $R\sin\langle\varphi\rangle = 0.175$ m. In CC operation, $j_i(\varphi)$ showed a single peak at the thruster central axis, and the rotation radius should be smaller than that of EC operation. Because of the larger rotation radius, EC operation showed higher α than that of CC operation (see Table 3). For further understanding of thrust generation in the electrostatic–magnetic hybrid acceleration, plasma diagnostics such as an ion velocity measurement is required, which is out of scope of the present study.

D. Plasma Properties

To understand the effects of cathode position on ion beam characteristics, plasma diagnostics using the double probe and the emissive probe were conducted under the same operating conditions ($\dot{m}_a = 1.4$ mg/s, $\dot{m}_c = 0.48$ mg/s, $B = 315$ mT, $V_d = 250$ V) except for hollow cathode position. Figures 14a–14c show n_e, T_e, and V_s distributions in CC operation. Among the probe measurement region, the high-density region is located in the vicinity of the hollow cathode exit. At $(z, r) = (5\text{ mm}, 0\text{ mm})$, n_e reached 2.5×10^{19} m^{-3} and monotonically decreased in the downstream direction. The high electron temperature region was concentrated in the vicinity of the anode. In this region, T_e reached more than 10 eV, and the maximum electron temperature was 12 eV at $(z, r) = (5\text{ mm}, 12.5\text{ mm})$. Outside the discharge channel, T_e decreased to less than 3 eV, and it maintained that value in the downstream region. The magnetic field configuration strongly affected the V_s distribution, such that V_s had a constant value along the magnetic lines of force. Although V_d was set to 250 V, the maximum V_s was 159 V at $(z, r) = (5\text{ mm}, 12.5\text{ mm})$. Because V_s rapidly decreased to the radial inward direction, generated ions were electrostatically accelerated toward the central axis. This ion focusing is shown in Fig. 13a, and j_i had a maximum value around $\varphi = 0$ deg.

Figures 15a–15c show n_e, T_e, and V_s distributions in EC operation. A separatrix of the applied magnetic field roughly exists near $z \approx 25$ mm, and generated plasma was also confined in $z \leq 25$ mm. The highest n_e was 5.5×10^{18} m^{-3} at $(z, r) = (20\text{ mm}, 2.5\text{ mm})$. While $z \leq 25$ mm, n_e was maintained on the order of 10^{18} m^{-3}; however, beyond $z = 25$ mm, n_e monotonically decreased in the downstream region. As electrons were well confined by magnetic lines of force, there was a local low-density region around $(z, r) = (10\text{ mm}, 10\text{ mm})$. Unlike CC operation, T_e was not distributed along the magnetic lines of force, instead showed locally higher values, up to 25 eV at $(z, r) = (10\text{ mm}, 0\text{ mm})$. The high T_e region was concentrated in $10\text{ mm} \leq z \leq 20$ mm, and in other regions, T_e remained at approximately 5 eV. The magnetic field separatrix affected the distribution of V_s similar to how it did in the distribution of n_e. In $z \leq 25$ mm, V_s was greater than 160 V; however, beyond $z = 25$ mm, V_s rapidly decreased monotonically in the downstream region.

In CC operation, the cathode potential was almost maintained on the central axis. In EC operation, emitted electrons from the hollow cathode were trapped by the magnetic field at the vicinity of the hollow cathode. Hence, a large portion of the electrons could not reach the central axis, and plasma properties showed strong dependence on the hollow cathode position. These different plasma properties affect the thruster operating characteristics. With constant mass-flow rate and input power, CC operation showed low discharge voltage × large discharge current, and EC operation showed high discharge voltage × small discharge current. As shown in Fig. 11, $J_i/(e\dot{m}_t/m_i)$ reached unity in both cathode locations. Hence, with same V_d and $\dot{m}_a$, the difference of J_i/J_d depends only on the difference of J_d. The J_d values, or the electron motions under magnetic field, were characterized by an electron-Hall parameter, which is defined as the electron-cyclotron frequency $f_{c,e}$ ratio against to the collision frequency $f_{e,i}$. Higher electron-Hall parameter means that electrons are trapped by the magnetic field and diffusion across

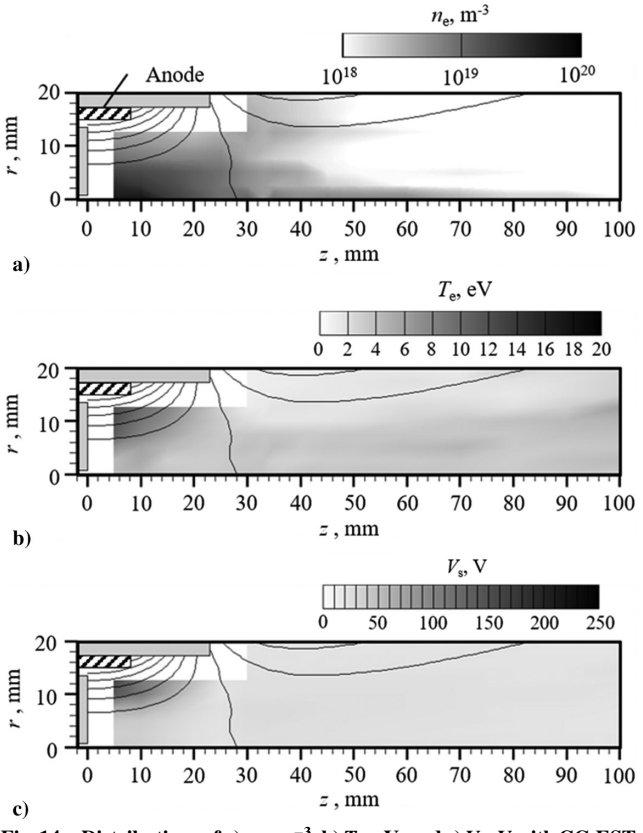

Fig. 14 Distributions of a) n_e, m^{-3}, b) T_e, eV, and c) V_s, V with CC-EST, $\dot{m}_a = 1.4$ mg/s, $\dot{m}_c = 0.48$ mg/s, $B = 315$ mT, $V_d = 250$ V.

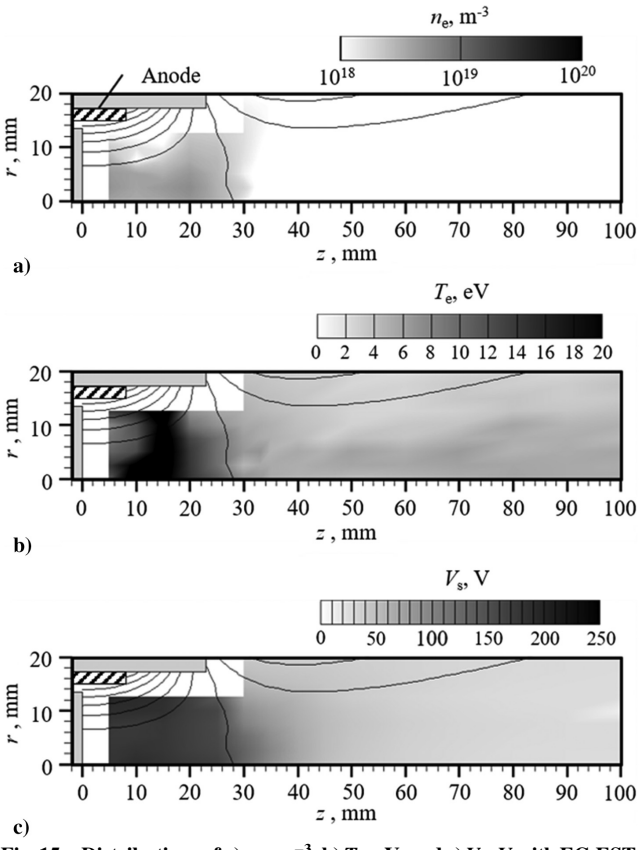

Fig. 15 Distributions of a) n_e, m^{-3}, b) T_e, eV, and c) V_s, V with EC-EST, $\dot{m}_a = 1.4$ mg/s, $\dot{m}_c = 0.48$ mg/s, $B = 315$ mT, $V_d = 250$ V.

the magnetic lines of force is suppressed. In $B = 315$ mT, $f_{c,e} = eB/m_e = 8.8 \times 10^9$ Hz. Assuming that electrons collide only with ions by a Coulomb collision, the Coulomb collision frequency $f_{e,i}$ is expressed as follows [23]:

$$f_{e,i} = \frac{\pi e^4 n_i}{(4\pi\varepsilon_0 m_i)^2 u_i^3} \log\Lambda \tag{13}$$

Here, u_e is electron thermal velocity, $\Lambda = 12\pi n_e \lambda_D^3$, and λ_D is Debye length. Substituting n_e and T_e values at $(z, r) = (5\text{ mm}, 0\text{ mm})$ as a representative value, $f_{e,i} = 1.6 \times 10^8$ Hz for CC operation and 2.8×10^6 Hz for EC operation. Using these frequencies, the electron-Hall parameter was 55 and 3140 for CC and EC operation, respectively. Because of the higher electron-Hall parameter in EC operation, electron diffusion across the magnetic lines of force was suppressed and J_d remained smaller than that of CC operation. As a result, EC operation showed a much higher ion to discharge current ratio than that of CC operation. Owning to the electromagnetic acceleration, electron back current contributed to generating thrust as shown in Table 3. Under the same $\dot{m}_a$ of 2.0 mg/s and P_a of 640 W in $B = 315$ mT, J_i/J_d was 0.39 and 0.68 for CC and EC operation, respectively, while $F = 21$ mN in both cathode locations. As a result, thrust performances were similar in both cathode positions. The electrostatic–magnetic hybrid plasma acceleration can be a strong advantage, especially for increasing thrust density. The point of the hybrid plasma acceleration is that, by combining electromagnetic acceleration, the generated thrust can increase even with lower electron-Hall parameter operation. Within the experimental conditions investigated in this study, the maximum thrust density was 52 and 47 N/m^2 for CC and EC operation, respectively. Compared with conventional electrostatic thrusters, ESTs have higher thrust density than that of cylindrical Hall thruster (22 N/m^2 [24]), HEMP thruster (37 N/m^2 [25]), cusped field thruster (15 N/m^2 [26]), and comparable with state-of-the-art Hall thruster SPT-140 (50 N/m^2 [23]). This high-thrust-density capability due to the electrostatic–magnetic hybrid plasma acceleration should be further improved in further studies.

IV. Conclusions

This study investigated two different hollow cathode positions, central and external, in a diverging-magnetic-field electrostatic thruster, which has a diverging magnetic field between the ring anode and the hollow cathode. Measurements comparing the operation of the central and external hollow cathode under an identical diverging magnetic field have shown some similarities and differences in thruster operation characteristics. Based on discharge current and direct thrust measurements, the electrostatic and magnetic hybrid plasma acceleration was observed in CC and even in EC operation, especially when $B \leq 315$ mT. Both cathode positions shared the same plasma acceleration mechanisms. However, the operating points were different: low discharge voltage × large discharge current in CC operation and high discharge voltage × small discharge current in EC operation. This difference comes from electron-Hall parameter; the estimated electron-Hall parameter was about 50 in CC operation, which was much lower than that of 3000 in EC operation. The point of electrostatic–magnetic hybrid accelerations is that, by combining electromagnetic acceleration, the generated thrust can increase even with lower electron-Hall parameter operation. Therefore, CC operation with larger discharge current and lower discharge voltage showed the same level of thrust and thrust performances as well as EC operation with smaller discharge current and higher discharge voltage. Because of the hybrid plasma acceleration method, thrust density reached 50 N/m^2, which is comparable or even higher with respect to conventional electrostatic thrusters.

Acknowledgments

This research was supported by Japan Society for the Promotion of Science (JSPS) KAKENHI Grant No. 18H03813. The authors thank A. Saito from the Technical Division, Nagoya University, for his valuable technical assistance.

References

[1] Martibez-Sanchez, M., and Pollard, J. E., "Spacecraft Electric Propulsion—An Overview," *Journal of Propulsion and Power*, Vol. 14, No. 5, 1998, pp. 688–699. https://doi.org/10.2514/2.5331

[2] Rathsman, P., Kugelberg, J., Bodin, P., Racca, G. D., Foing, B., and Stagnaro, L., "SMART1: Development and Lessons Learnt," *Acta Astronautica*, Vol. 57, Nos. 2–8, May 2005, pp. 455–468. https://doi.org/10.1016/j.actaastro.2005.03.041

[3] Oh, D. Y., Snyder, J. S., Goebel, D. M., Hofer, R. R., and Randolph, T. M., "Solar Electric Propulsion for Discovery-Class Missions," *Journal of Propulsion and Power*, Vol. 51, No. 6, 2014, pp. 1822–1835. https://doi.org/10.2514/1.A32889

[4] Snyder, J. S., Goebel, D. M., Hofer, R. R., and Polk, J. E., "Performance Evaluation of the T6 Ion Engine," *Journal of Propulsion and Power*, Vol. 28, No. 2, 2012, pp. 371–379. https://doi.org/10.2514/1.B34173

[5] Kunning, G. X., and Mitchell, L. R. W., "Effect of External Cathode Azimuthal Position on Hall-Effect Thruster Plume and Diagnostics," *Journal of Propulsion and Power*, Vol. 30, No. 2, 2014, pp. 371–379. https://doi.org/10.2514/1.B34980

[6] Hofer, R. R., Johnson, L. K., Goebel, D. M., and Wirz, R. E., "Effects of Internally Mounted Cathodes on Hall Thruster Plume Properties," *IEEE Transactions on Plasma Science*, Vol. 36, No. 5, 2008, pp. 2004–2014. https://doi.org/10.1109/TPS.2008.2000962

[7] Ding, Y., Li, H., Li, P., Jia, B., Wei, L., Su, H., Sun, H., Wang, L., and Yu, D., "Effects of Relative Position Between Cathode and Magnetic Separatrix on the Discharge Characteristic of Hall Thruster," *Vacuum*, Vol. 154, Aug. 2018, pp. 167–173. https://doi.org/10.1016/j.vacuum.2018.05.005

[8] Harada, S., Baba, T., Uchigashima, A., Yokota, S., Iwakawa, A., Sasoh, A., Yamazaki, T., and Shimizu, H., "Electrostatic Acceleration of Helicon Plasma Using a Cusped Magnetic Field," *Applied Physics Letters*, Vol. 105, No. 19, 2014, Paper 194101. https://doi.org/10.1063/1.4900423

[9] Ichihara, D., Iwakawa, A., and Sasoh, A., "Effects of Magnetic Field Profile Near Anode on Ion Acceleration Characteristics of a Diverging Magnetic Field Electrostatic Thruster," *Journal of Applied Physics*, Vol. 122, No. 4, 2017, Paper 043302. https://doi.org/10.1063/1.4995286

[10] Sasoh, A., Mizutani, K., and Iwakawa, A., "Electrostatic/Magnetic Ion Acceleration Through a Slowly Diverging Magnetic Nozzle Between a Ring Anode and an On-Axis Hollow Cathode," *AIP Advances*, Vol. 7, No. 6, 2017, Paper 065204. https://doi.org/10.1063/1.4985380

[11] Sasoh, A., Kasuga, H., Nakagawa, Y., Matsuba, T., Ichihara, D., and Iwakawa, A., "Electrostatic-Magnetic Hybrid Thrust Generation in Central-Cathode Electrostatic Thruster (CC-EST)," *Acta Astronautica*, Vol. 152, Nov. 2018, pp. 137–145. https://doi.org/10.1016/j.actaastro.2018.07.052

[12] Nagao, N., Yokota, S., Komurasaki, K., and Arakawa, Y., "Development of a Two-Dimensional Dual Pendulum Thrust Stand for Hall Thrusters," *Review of Scientific Instruments*, Vol. 78, No. 11, 2007, Paper 115108. https://doi.org/10.1063/1.2815336

[13] XXXXX.

[14] Lieberman, M. A., and Lichtenberg, A. J., *Principles of Plasma Discharges and Materials Processing*, 2nd ed., Wiley, Hoboken, NJ, 2005, p. 302. https://doi.org/10.1002/0471724254

[15] Brown, D. L., Larson, C. W., Beal, B. E., and Gallimore, A. D., "Methodology and Historical Perspective of a Hall Thruster Efficiency Analysis," *Journal of Propulsion and Power*, Vol. 25, No. 6, 2009, pp. 1163–1177. https://doi.org/10.2514/1.38092

[16] Johnson, E. O., and Malter, L., "A Floating Double Probe Method for Measurements in Gas Discharge," *Physical Review*, Vol. 80, No. 1, 1950, pp. 58–68. https://doi.org/10.1103/PhysRev.80.58

[17] Smith, B. A., and Overzet, L. J., "Improvements to the Floating Double Probe for Time-Resolved Measurements in Pulsed RF Plasmas," *Review of Scientific Instruments*, Vol. 69, No. 3, 1998, pp. 1372–1377. https://doi.org/10.1063/1.1148768

[18] Hutchnson, I. H., *Principles of Plasma Diagnostics*, 2nd ed., Cambridge Univ. Press, Cambridge, England, U.K., 2002. pp. 65–67. https://doi.org/10.1017/CBO9780511613630

[19] Fruchtman, A., Zoler, D., and Makrinich, G., "Potential of an Emissive Cylindrical Probe in Plasma," *Physical Review E*, Vol. 84, No. 2, 2011, Paper 025402.
https://doi.org/10.1103/PhysRevE.84.025402

[20] Raitses, Y., Keidar, M., Staack, D., and Fisch, N. J., "Effects of Segmented Electrode in Hall Current Plasma Thrusters," *Journal of Applied Physics*, Vol. 92, No. 9, 2002, pp. 4906–4911.
https://doi.org/10.1063/1.1510556

[21] Staack, D., Raitses, Y., and Fisch, N. J., "Shielded Electrostatic Probe for Nonperturbing Plasma Measurements in Hall Thrusters," *Review of Scientific Instruments*, Vol. 75, No. 2, 2004, pp. 393–399.
https://doi.org/10.1063/1.1634353

[22] Fradkin, D. B., Blackestock, A. W., Roehling, D. J., Stratton, T. F., Williams, M., and Liewer, K. W., "Experiments Using a 25-kW Hollow Cathode Lithium Vapor MPD Arcjet," *AIAA Journal*, Vol. 8, No. 5, 1970, pp. 886–894.
https://doi.org/10.2514/3.5783

[23] Goebel, D. M., and Katz, I., *Fundamentals of Electric Propulsion: Ion and Hall Thrusters*, Wiley, Hoboken, NJ, 2008.
https://doi.org/10.1002/9780470436448

[24] Smimov, A., Raitses, Y., and Fisch, N. J., "Parametric Investigation of Miniaturized Cylindrical and Annular Hall Thrusters," *Journal of Applied Physics*, Vol. 92, No. 5, 2002, pp. 5673–5679.
https://doi.org/10.1063/1.1515106

[25] Koch, N., Harmann, H. P., and Komfeld, G., "Status of THALES High Efficiency Multi Stage Plasma Thruster Development for HEMP-T 3050 and HEMP-T 30250," *Proceedings of the 30th International Electric Propulsion Conference*, Electric Rocket Propulsion Soc., IEPC Paper 2007-110, Florence, Italy, 2007.

[26] Hu, P., Liu, H., Gao, Y., Mao, W., and Yu, D., "An Experimental Study of the Effect of Magnet Length on the Performance of a Multi-Cusped Field Thruster," *Journal of Physics D: Applied Physics*, Vol. 49, No. 28, 2016, Paper 285201.
https://doi.org/10.1088/0022-3727/49/28/285201

G. G. Spanjers
Associate Editor

Queries

1. AU: Please check that the copyright (©) type is correct. Please note that the code will be added upon publication.
2. AU: The sentence “In ion thrusters, ions are extracted by applying . . . ” has been edited for clarity. Please check.
3. AU: Please provide missing Reference [13].
4. AU: Please provide page range or chapter number for Ref. [23].

Funding Information

The following research funding sources have been associated with your manuscript:

- Japan Society for the Promotion of Science; Award no. 18H03813;
  Funder ID http://dx.doi.org/10.13039/501100001691

Funding sources listed here can be 1) research grants from outside agencies or organizations or 2) if an author is employed by a U.S. government agency that directly funded this research, this employer also may be listed here as a funding agency. Please confirm that this information is complete and correct for all authors. Edit the Funding Data/Acknowledgments section of your paper if you have changes to funding agency names or grant numbers. Use the funder’s full and official name.